

# Butylamine-Catalyzed Synthesis of Nanocrystal Inks Enables Efficient Infrared CQD Solar Cells

Junghwan Kim, Olivier Ouellette, Oleksandr Voznyy, Mingyang Wei, Jongmin Choi, Min-Jae Choi, Jea Woong Jo, Se-Woong Baek, James Fan, Makhsud I. Saidaminov, Bin Sun, Peicheng Li, Dae-Hyun Nam, Sjoerd Hoogland, Zheng-Hong Lu, F. Pelayo García de Arquer, and Edward H. Sargent\*

The best-performing colloidal-quantum-dot (CQD) photovoltaic devices suffer from charge recombination within the quasi-neutral region near the back hole-extracting junction. Graded architectures, which provide a widened depletion region at the back junction of device, could overcome this challenge. However, since today's best materials are processed using solvents that lack orthogonality, these architectures have not yet been implemented using the best-performing CQD solids. Here, a new CQD ink that is stable in nonpolar solvents is developed via a neutral donor ligand that functions as a phase-transfer catalyst. This enables the realization of an efficient graded architecture that, with an engineered band-alignment at the back junction, improves the built-in field and charge extraction. As a result, optimized IR CQD solar cells ( $E_g \approx 1.3$  eV) exhibiting a power conversion efficiency (PCE) of 12.3% are reported. The strategy is applied to small-bandgap (1 eV) IR CQDs to augment the performance of perovskite and crystalline silicon (cSi) 4-terminal tandem solar cells. The devices show the highest PCE addition achieved using a solution-processed active layer: a value of +5% when illuminated through a 1.58 eV bandgap perovskite front filter, providing a pathway to exceed PCEs of 23% in 4T tandem configurations with IR CQD PVs.

Colloidal quantum dots (CQDs) are attractive semiconductor materials in view of their readily tunable bandgap, low-temperature solution-processing, and ambient stability.<sup>[1–3]</sup> These advantages have enabled the realization of efficient CQD thin-film optoelectronic devices such as photodetectors,<sup>[4,5]</sup> transistors,<sup>[6]</sup> light-emitting diodes,<sup>[7]</sup> and photovoltaics (PVs).<sup>[8,9]</sup> Their ability to harvest photons in the infrared (IR) region of the solar spectrum beyond the absorption edge of crystalline silicon (cSi) ( $E_g = 1.1$  eV) and perovskites ( $E_g = 1.58$  eV) makes them promising candidates for tandem photovoltaic devices.<sup>[1,10]</sup>


The power conversion efficiency (PCE) of IR CQD solar cells needs to be improved further to move in the direction of commercial viability. Significant advances have been made in the synthesis, inorganic halide passivation, solution-phase ligand exchange, and interface engineering of CQDs;<sup>[11–13]</sup> yet crucial issues remain to be solved. State-of-art

CQD PV is based on a depleted heterojunction architecture that relies on a solution-phase exchanged CQD ink employing MX ( $M = \text{Pb}, \text{Cd}; X = \text{Br}, \text{I}, \text{Se}$ )-passivation.<sup>[11,14,15]</sup> This structure consists of an n-type metal oxide:PbS CQD light-absorbing layer:hole-transport layer, the latter consisting of thiol-treated CQDs. In these devices, the majority of free carriers are extracted from the depletion region near the front n-type metal oxide/PbS interface with the aid of the internal electric field. In contrast, the quasi-neutral region at the back junction of the device is little affected by the electric field and charge extraction relies on diffusion of the free carriers. This problem becomes more acute still at the maximum power point and also for thick absorbing layers, since charge recombination in the quasi-neutral region limits device performance.<sup>[16]</sup>

One promising strategy to facilitate charge extraction from the quasi-neutral region involves the use of graded band alignment, achieved for example by stacking different sized CQDs in one device.<sup>[17–20]</sup> Such graded architectures enhance the built-in electric field at the back junction, thereby diminishing the quasi neutral region and reducing charge recombination.

Dr. J. Kim,<sup>[†]</sup> O. Ouellette, Prof. O. Voznyy, M. Wei, Dr. J. Choi, Dr. M.-J. Choi, Dr. J. W. Jo,<sup>[††]</sup> Dr. S.-W. Baek, J. Fan, Dr. M. I. Saidaminov, Dr. B. Sun, Dr. D.-H. Nam, Dr. S. Hoogland, Dr. F. P. García de Arquer, Prof. E. H. Sargent  
Department of Electrical and Computer Engineering  
University of Toronto  
10 King's College Road, Toronto, Ontario M5S 3G4, Canada  
E-mail: ted.sargent@utoronto.ca

P. Li, Prof. Z.-H. Lu  
Department of Materials Science and Engineering  
University of Toronto  
184 College Street, Toronto, Ontario M5S 3E4, Canada

 The ORCID identification number(s) for the author(s) of this article can be found under <https://doi.org/10.1002/adma.201803830>.

<sup>[†]</sup>Present address: Photo-electronic Hybrids Research Center, Korea Institute of Science and Technology (KIST), Seoul 02792, Korea

<sup>[††]</sup>Present address: Department of Energy and Materials Engineering, Dongguk University-Seoul, 04620 Seoul, Republic of Korea

DOI: 10.1002/adma.201803830

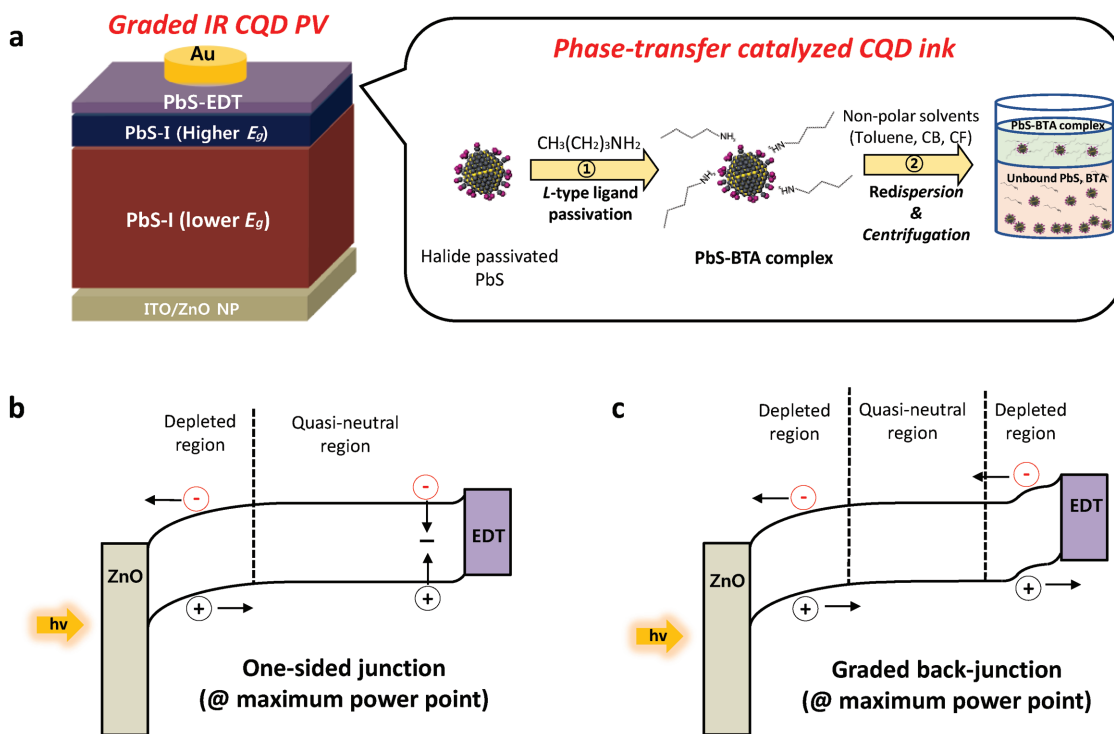


**Figure 1.** Graded IR CQD PV devices with phase-transfer catalyzed IR CQDs. a) Schematic illustration of device architecture for graded IR CQD PV and solvent engineering process of the halide passivated PbS CQDs in nonpolar solvents. b,c) Energy landscape of a standard solar cell (one-sided junction) (b) and a graded-junction device junction (c) at the maximum power point.

Previous attempts to realize graded CQD films relied on solid-state ligand exchanges that used layer-by-layer (LBL) CQD film assembly or centrifugal casting deposition employing organic-ligand-passivated CQDs.<sup>[19,20]</sup> Unfortunately, solid-state ligand exchanges and organic ligand passivation schemes are now known to limit device performance, and these effects combined account for a modest prior power conversion efficiency (PCE) record for graded CQD PV devices of 6.1%. Graded CQD devices that employ state-of-art solution-phase halide exchanges, which enable the highest-available IR CQD PV performance, remain to be explored.

The best-performing CQD inks are well-dispersed only in polar and amine solvents as a result of their strong interaction with the halide ions. However, the need for polar and amine solvents precludes the sequential stacking of high-quality CQD films, for the solvents will redisperse and otherwise damage underlying CQD films (Figure S1, Supporting Information).

Developing a halide-passivated CQD nonpolar ink will enable the construction of stacked graded architectures. This goal is rendered challenging by the weak interaction between nonpolar solvent molecules and halide ions. Film transfer has been explored as an option to achieve layer stacking,<sup>[21]</sup> but this method has shown limited reproducibility and a propensity to introduce interface defects.<sup>[22,23]</sup> In addition, prior ligand passivation strategies have often resulted in poor charge transport due to excess residual ligands in the CQD films. We reasoned that pursuing a new strategy that achieves high-quality and stable CQD inks dispersed in nonpolar solvents without the deleterious incorporation of residual ligands into films contribute to the realization of ever-more-efficient CQD PV.

Here, we began by developing a facet-independent ligand-exchange strategy that, by employing L-type organic ligands as phase-transfer catalysts, would enable the realization of high-quality CQD inks that are colloiddally stable in nonpolar solvents. Using this strategy, we developed high-efficiency graded IR-CQD PV devices with engineered band alignment at the back junction of the devices that improved charge extraction efficiency and open circuit voltage ( $V_{oc}$ ). We then explored the potential of the graded architecture both for large-bandgap ( $E_g \approx 1.3$  eV) and small-bandgap ( $E_g \approx 1$  eV) CQDs. The best-performing large-bandgap CQD devices exhibited a PCE of 12.3%. Graded IR PVs with smaller bandgap CQDs showed an additional PCE of +5.0% on top of perovskite (790 nm bandgap) and +1.1% on top of Si (1100 nm bandgap), respectively. This opens the door to the realization of solution-processed tandem photovoltaic solar with PCEs exceeding 23.3% of the current-best single junction perovskite solar cell.<sup>[24]</sup>

**Figure 1a** illustrates the graded PbS PV architecture with a device configuration of indium tin oxide (ITO)/ZnO nanoparticles/PbS (lower bandgap,  $E_g$ )/PbS (higher  $E_g$ )/1,2-ethanedithiol (EDT)-treated PbS/Au, where the two different-sized PbS CQDs formed a back-junction. Both the PbS CQD layers were passivated with PbX ( $X = \text{I}, \text{Br}$ ) using a solution-phase ligand exchange. In contrast with the typical one-sided junction configuration (Figure 1b), the graded architecture introduces a wider  $E_g$  CQD layer on top of the lower  $E_g$  CQD film, thereby forming a widened, depleted junction at the back of the device and reinforcing the built-in field in this region (Figure 1c). Device modeling using SCAPS confirmed the benefits of the graded architecture (Figure S2, Supporting Information).

The development of halide-passivated PbS CQD inks dispersed in nonpolar solvents is a prerequisite for ink-based graded devices, as the presence of amines and polar solvents would otherwise dissolve the underlying CQD layers (Figure S1, Supporting Information). Due to the weak interaction between the nonpolar solvent molecules and halide ions on the CQD surface, an added element is needed to disperse the CQDs in the nonpolar solvents. The host-guest coordination of metal-chalcogenide-complex-capped nanocrystals (NCs) with macrocyclic ether (e.g., crown ether) was previously proposed to tune the solubility of NCs.<sup>[25]</sup> We instead sought an approach wherein the additives transiently help to disperse the nanocrystals for ink formation, but are then removed in order to avoid impeding efficient charge transport. We introduced the neutral donor L-type ligand<sup>[26]</sup> butylamine (BTA) as a phase-transfer catalyst to enable the dispersion of CQDs in nonpolar solvents. We posit that the lone pair electrons of the primary amine group and the moderate length of the C–H alkyl chain allow the interaction of BTA with both the polar surface of CQDs and nonpolar solvents. Its low boiling point (78 °C) ensures facile removal in the final films via thermal annealing.

We dissolved the halide-passivated PbS dots using a small amount of BTA to make highly concentrated inks (10 mg/10  $\mu$ L) of PbS–BTA complexes, unbound PbS and BTA solvent (Figure 1a). We then redispersed the mixture in nonpolar solvents with a volume ratio of 1:10. After centrifuging, the lighter upper phase consists of BTA-capped CQDs in a nonpolar solvent and is ready for film formation.

The PbS–BTA complex is a key intermediate phase to enable nonpolar stable CQD inks that lead to high-quality CQD solids. We confirmed this using Fourier-transform infrared spectroscopy (FT-IR) (Figure 2a and Figure S3, Supporting Information). We prepared the as-deposited wet PbS film to check for the presence of the PbS–BTA complex. The strong C–H stretching at 2960  $\text{cm}^{-1}$  and N–H<sub>2</sub> bending at 1648  $\text{cm}^{-1}$  reveal the presence of BTA molecules in the as-deposited CQD film (Figure S3a, Supporting Information). Notably, the N–H bending peak at 1600  $\text{cm}^{-1}$  of pure BTA solvent shifts to a lower energy in the CQD film due to the interaction between Lewis base BTA and Lewis acid PbX<sub>2</sub> on the CQDs. This indicates the formation of CQD–BTA complexes.<sup>[27]</sup> The BTA molecules are then eliminated via thermal annealing at 70 °C in a N<sub>2</sub> atmosphere; the role of BTA is catalytic, helping to disperse the CQDs in nonpolar solvent inks without being ultimately incorporated into films. The resultant CQD films processed from the various type of nonpolar solvents, such as chlorobenzene (CB), toluene, ethyl ether, and chloroform (CF), exhibit excellent film uniformity (Figure S3b, Supporting Information). In particular, we found that CB and toluene are the optimal solvents to realize CQD ink formulations with  $\approx$ 100% yield of phase-transfer to a nonpolar solvent and excellent films (Figures S4 and S5, and Table S2, Supporting Information). The narrow exciton peak, with a full-width-at-half-maximum of  $\approx$ 83 meV, showcases that the spatial uniformity of quantum dots is preserved for the CB-processed CQD film (Figure 2b), thereby leading to efficient CQD PV devices using the CQD inks (Figure S6, Supporting Information).

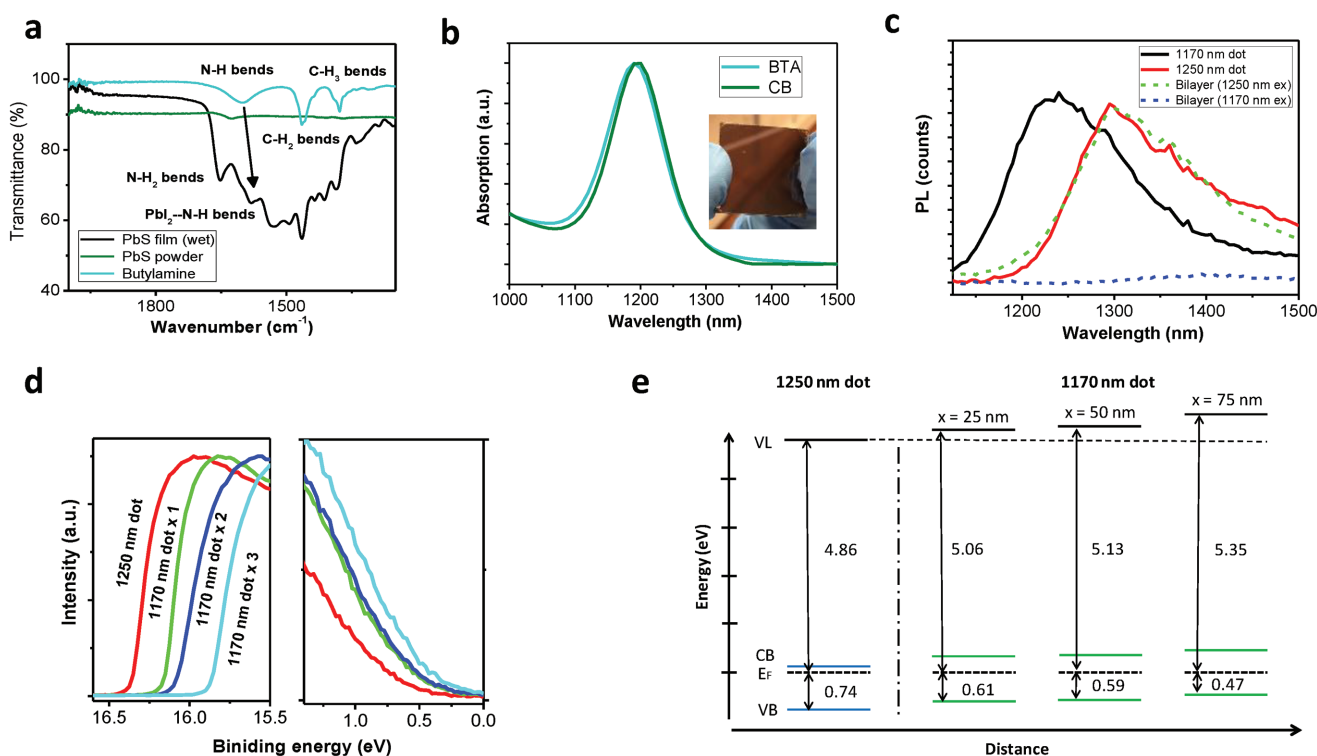


**Figure 2.** Characterization of phase-transfer catalyzed IR CQD films. a) FT-IR spectra of as-deposited PbS film, PbS powder, and pure butylamine solvents. b) Absorption spectra of IR CQD films processed from butylamine (BTA) and chlorobenzene (CB) solvents. (Inset) IR CQD film processed from CB solvent. c) Steady-state PL spectra of single PbS films with first exciton peaks of 1170 and 1250 nm, and 1250 nm PbS/1170 nm PbS bilayers. The bilayers were excited by the light illuminated from 1250 nm PbS or 1170 nm PbS, respectively. d) UPS spectra and e) corresponding energy level from the UPS results of 1250 nm PbS single film and 1–3 layers of 1170 nm PbS films on top of the 1250 nm PbS film.

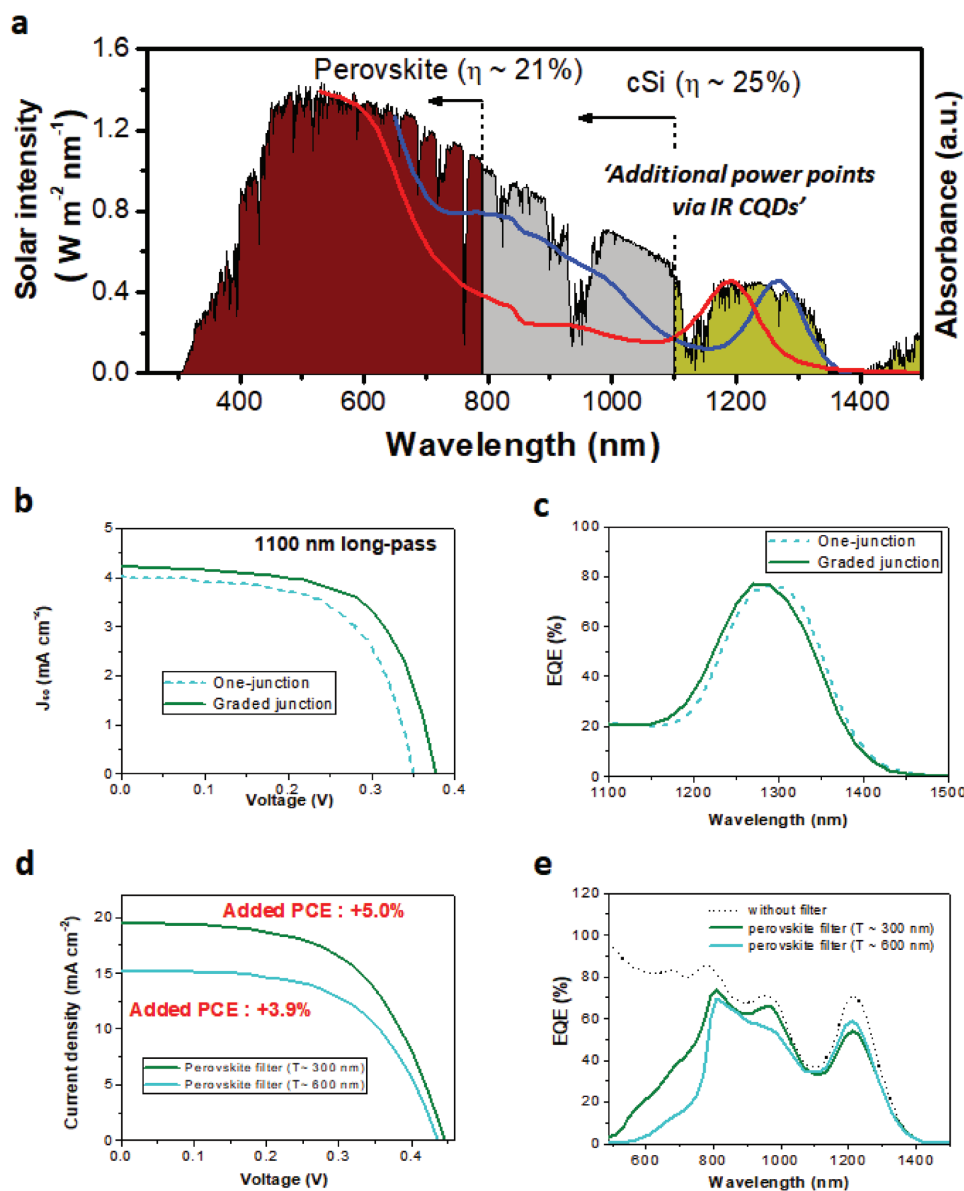


**Figure 3.** Graded IR CQD ( $E_g \approx 1$  eV) solar cell for 4T tandem with cSi and perovskite. a) Solar spectrum and absorption of small- $E_g$  (1 and 1.13 eV) IR CQD films. Absorption onsets of perovskite and cSi are indicated as dotted lines. b) Current density–voltage ( $J$ – $V$ ) characteristics, c) EQE spectra of the IR CQD PV devices with one-junction and graded junction under 1100 nm long-pass filter (cSi filter). d)  $J$ – $V$  characteristics and e) EQE spectra of thick IR CQD PV device under perovskite filters ( $E_g = 1.58$  eV) with 300 and 600 nm thickness, respectively.

We first investigated the band-alignment tunability of engineered CQD inks. Phase-transfer catalyzed PbS CQD inks having a first exciton peak ( $\lambda_{ex}$ ) at 1170 nm were deposited onto the PbS film with  $\lambda_{ex} \approx 1250$  nm to prepare the multi-stacked PbS films (Figure S7, Supporting Information). The steady-state photoluminescence (PL) spectra of the 1250 nm PbS/1170 nm PbS bilayer showed that when 1170 nm CQDs are excited, PL quenching occurs (Figure 2c). This indicates that efficient charge transfer takes place from wider bandgap 1170 nm PbS to 1250 nm PbS CQDs. Ultraviolet photoelectron spectroscopy (UPS) spectra (Figure 2d) and relevant energy levels (Figure 2e) from the UPS results indicate the formation of type-II band alignment, which is beneficial for

the efficient charge extraction at the back-junction and well consistent with the PL data.

We then sought to take advantage of the nonpolar CQD inks to implement a graded device architecture that improves charge extraction. We fabricated small bandgap ( $\approx 1$  eV) IR CQD PV devices. These CQDs are promising candidates to realize 4-terminal (4T) tandem devices complementing perovskite and cSi PV by extending their absorption beyond 800 and 1100 nm (Figure 3a). Based on detailed-balance calculation for the 4T tandem devices, we chose PbS CQDs with a first exciton peak ( $\lambda_{ex}$ ) around 1250 nm as the main photoactive layer due to their optimal  $E_g$  for 4T tandems with perovskites and cSi (Figure S8, Supporting Information).<sup>[10,28,29]</sup> Slightly wider bandgap PbS

CQDs with a shallower electron affinity and an exciton peak at 1160 nm were used to improve charge extraction at the back junction of the device.

To evaluate the potential of graded CQD IR solar cells enabled by the nonpolar ink to provide additional power points on top of perovskite and silicon devices, we characterized the photovoltaic performance using corresponding long-pass filters. The photovoltaic performance after a 1100 nm long-pass filter, simulating a Si solar cell, is shown in Figure 3b and summarized in Table S1 (Supporting Information). Control devices with a standard depleted architecture exhibit an added PCE of +0.85%, a short-circuit current density ( $J_{sc}$ ) of  $4.0 \text{ mA cm}^{-2}$ , an open circuit voltage ( $V_{oc}$ ) of  $0.35 \pm 0.01 \text{ V}$ , and a fill factor (FF) of  $61 \pm 1\%$ . Graded devices, on the other hand, exhibited a superior PCE of +1.0%, stemming from a higher  $J_{sc}$  of  $4.2 \text{ mA cm}^{-2}$ , a slightly larger  $V_{oc}$  of  $0.37 \pm 0.01 \text{ V}$ , and a larger FF of  $64 \pm 1\%$ . The main contributions to the enhanced PCE are the higher  $V_{oc}$  and FF compared to standard one-junction devices, in agreement with an increased built-in potential and improved charge extraction efficiency at the back of the graded device, confirmed via SCAPS simulations (Figure S2, Supporting Information).<sup>[28]</sup> This is also supported by the high EQE at the exciton peak ( $\lambda_{ex} \approx 1280 \text{ nm}$ ) of 78% for graded devices, which is the highest value among the reported small- $E_g$  (<1 eV) IR CQD devices (Figure 3c). The higher  $V_{oc}$  stems from a larger built-in potential of the graded device ( $V_{bi} \approx 0.60 \text{ V}$ ) versus standard devices (0.55 V), which we obtained using Mott–Schottky analysis of capacitance–voltage measurements (Figure S9, Supporting Information). Further optimization of the graded IR devices resulted in a new record PCE of 1.1% for 1100 nm filtered solar illumination (Figure S10, Supporting Information), a 35% improvement relative to the previous record PCE of 0.8%,<sup>[10]</sup> providing a potential PCE > 26% in cSi/IR CQD 4T tandem solar cells.

We then investigated the potential of the graded devices as the back cell for perovskite solar cells, also in a 4T tandem configuration. Two different thicknesses (300 and 600 nm) of perovskite long-pass filters ( $E_g \approx 1.58 \text{ eV}$ ) were prepared with a composition of formamidinium methylammonium cesium lead halides ( $\text{FA}_{0.81}\text{MA}_{0.14}\text{Cs}_{0.05}\text{PbI}_{2.55}\text{Br}_{0.45}$ ) and used for the  $J$ – $V$  and EQE measurements (Figure S11, Supporting Information).<sup>[30,31]</sup> In this configuration, the light harvesting beyond 800 nm needs to be maximized in the CQD layer, which entails

increasing the thickness of the active layer (Figure S12, Supporting Information).

We then sought to take advantage of the benefits of the graded architecture in the much-needed IR regime and employed nonpolar inks to fabricate small  $E_g$  (1 eV) IR PbS CQD thick devices (600 nm) to improve IR absorption and charge extraction (Figure S13, Supporting Information). The thick IR CQD devices show a  $J_{sc}$  of  $37.4 \text{ mA cm}^{-2}$  and a PCE of 9.5% under full spectrum AM 1.5G illumination (Figure S13a, Supporting Information)—this represents a record PCE for full AM1.5G operation for these low-bandgap CQDs. Thick IR CQD solar cells exhibited +5.0% PCE points (corresponding to  $V_{oc}$ :  $0.45 \pm 0.01 \text{ V}$ ,  $J_{sc}$ :  $19.6 \text{ mA cm}^{-2}$ , FF:  $57 \pm 1\%$ ) and +3.9% ( $V_{oc}$ :  $0.44 \pm 0.01 \text{ V}$ ,  $J_{sc}$ :  $15.3 \text{ mA cm}^{-2}$ , FF:  $58 \pm 1\%$ ) using 300 and 600 nm thick filters, respectively (Figure 3d). These values are the highest PCEs among reported perovskite-filtered IR CQD PV devices.<sup>[28]</sup> The high IR EQE values, above 70% up to a wavelength of 1000 nm and  $\approx 40\%$  at 1100 nm, account for the observed high  $J_{sc}$  of the filtered devices (Figure 3e). They showcase the benefits of the graded architecture in improving charge extraction.

To determine more realistic efficiencies of the 4-T tandem devices, we used SCAPS to estimate the PCE of single-pass, semitransparent perovskite solar cells (600 nm thick), i.e., without the additional absorption provided by the reflective back contact. (Figure S14 and Table S3, Supporting Information). The simulated PCE of standard perovskite double-pass device with an Au top electrode was 21.4% ( $V_{oc}$ :  $1.16 \pm 0.01 \text{ V}$ ,  $J_{sc}$ :  $22.5 \text{ mA cm}^{-2}$ , FF:  $82 \pm 1\%$ ), matching well the optimized experimental values (PCE = 21.5%) from our laboratory. By assuming a transparent top contact, we obtain a PCE of 19.1% ( $V_{oc}$ :  $1.16 \pm 0.01 \text{ V}$ ,  $J_{sc}$ :  $20.4 \text{ mA cm}^{-2}$ , FF:  $81 \pm 1\%$ ) for the semitransparent perovskite solar cell. This indicates a potential pathway to PCE of 23% in a 4T tandem configuration with IR CQD PVs (combined PCEs of  $19.1\% + 3.9\% = 23\%$ ), which is comparable to the current-best perovskite-perovskite 4T tandem.<sup>[32]</sup> The value can reach up to 25% with the incorporation of record single-junction perovskite solar cells and IR CQD PVs.

We also introduced the graded architecture strategy to improve upon state-of-art CQD devices ( $E_g \approx 1.3 \text{ eV}$ ). Optimized best-performing devices exhibited a PCE of 12.3% with a  $J_{sc}$  of  $28.8 \text{ mA cm}^{-2}$ , a  $V_{oc}$  of 0.63 V, and a FF of 68% (Figure 4b and

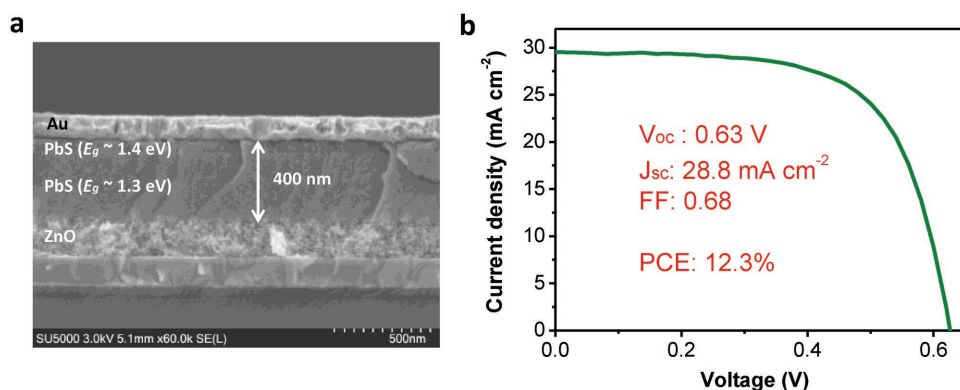


**Figure 4.** Graded IR CQD ( $E_g \approx 1.3 \text{ eV}$ ) solar cell performance. a) Cross-sectional SEM image and b)  $J$ – $V$  characteristics of graded IR CQD solar cell prepared using 1.3 eV bandgap PbS.

Figure S15, Supporting Information). This is the highest value among reported single junction PbS CQD PVs. Efficient charge extraction via enhanced built-in potential throughout the device with thicker light absorber layer ( $\approx 400$  nm) enabled higher currents and FF even for thick films, thereby leading to PCE improvement (Figure 4a).

In summary, we developed a new nonpolar CQD ink formulation in which L-type ligands render CQDs well-passivated and stable. Such a nonpolar high-quality ink allows stacking of CQD films with different optoelectronic properties, such as bandgap. We took advantage of this property to implement a graded IR-CQD PV architecture that improves the extraction of IR-photogenerated charges at the back junction of the device operating at maximum power point. This led to improvements in  $V_{oc}$  and FF and an IR EQE approaching 80%, which we exploited to implement IR CQD PV that show potential as the back cell in a 4T tandem PV configuration with perovskite and cSi solar cells. We demonstrated the addition of +1.1% PCE points on top of cSi and +5.0% on top of perovskite solar cells, which represent a new record among the reported values. The strategy also enabled the most efficient single-junction CQD ( $E_g \approx 1.3$  eV) solar cells reported to date with a PCE of 12.3%.

## Experimental Section

**Synthesis of PbS CQDs:** Lead-halide-passivated PbS CQDs were synthesized by solution-phase ligand-exchange process with oleic-acid-capped CQDs (OA-CQDs) as described in a previous report.<sup>[11]</sup> In the case of small- $E_g$  ( $\approx 1$  eV) CQDs, solution of lead halides (0.5 mmol  $PbI_2$  and 0.11 mmol  $PbBr_2$ ) and 0.21 mmol NaAc dissolved in 5 mL dimethylformamide (DMF) was prepared for ligand exchange, and mixed with 5 mL of OA-CQDs (7 mg mL<sup>-1</sup> in octane). The mixed solution was vortexed for 5 min at room temperature to complete transfer of CQD toward DMF. The ligand-exchanged solution was washed three times with octane for removing remained residues. The washed CQDs precipitated by addition of 0.45 mL toluene, and the CQDs were totally separated by following centrifugation. After 10 min drying under vacuum, the CQDs were redispersed in butylamine (BTA):DMF (4:1 v/v) with desired concentrations for film deposition. For large- $E_g$  ( $\approx 1.3$  eV) CQDs, solution-phase ligand-exchange was performed by following reported method for IR CQD inks.<sup>[11]</sup> The only difference is that the CQDs were redispersed in butylamine (BTA):CsI (780 mg/10 mL DMF) (9:1 v/v) with desired concentrations for film deposition. After film deposition, the substrates were annealed at 70 °C for 5 min in an oven under nitrogen condition.

**Preparation of Nonpolar Dispersed PbS Inks:** The halide passivated PbS dots after drying under vacuum are dissolved by using small amount of BTA to make highly concentrated mixed inks (10 mg/10  $\mu$ L). Then, the high concentrated solution is transferred into tubes and centrifugated. Then, the centrifuged solution is redispersed in nonpolar solvents with a volume ratio of 1:10. The ratio can be varied. After centrifuging again, only upper part of solution is composed of PbS–BTA complex and used for film formation.

**Fabrication of IR CQD Solar Cells:** The lead halide passivated-PbS IR-CQDs dissolved in BTA:DMF (4:1 v/v) mixtures were spin-coated (2500 rpm for 30 s) on as-prepared ETL films (ZnO and AZO). The concentration of PbS inks was 30 mg/110  $\mu$ L (for 400 nm thick) and 30 mg/90  $\mu$ L (for 600 nm thick). For the graded devices, 1 or 2 layers of nonpolar dispersed PbS (higher  $E_g$ ) inks were deposited onto the prepared PbS (smaller  $E_g$ ) films. For the nongraded devices, 1 or 2 layers of nonpolar dispersed PbS inks with same dot size were deposited onto the prepared PbS films. After that, 1,2-ethanedithiol (EDT) treated PbS layer was spin-coated on the lead halide passivated-CQD layer following previously reported method. For the top electrode, 120 nm Au was thermally evaporated on the PbS CQD film.

**Perovskite Filters:** The perovskite filters were prepared by following the reported method.<sup>[31,33]</sup> In detail, formamidinium iodide (FAI), cesium iodide (CsI), methylammonium bromide (MABr), lead iodide ( $PbI_2$ ), and lead bromide ( $PbBr_2$ ) were dissolved in DMSO:DMF (1:4) mixture solution in the following molar ratios:  $PbI_2/PbBr_2 = 0.5:0.5$ ,  $CsI/FAI/MABr = 0.05:0.81:0.14$ , and  $(FAI + MABr + CsI)/(PbI_2 + PbBr_2) = 1:1$  to get the final concentration of 1.4 M (for 600 nm thick film) and 0.7 M (for 300 nm thick). The precursor solutions were processed onto the glass substrate as follows: the first step was 1000 rpm for 10 s with an acceleration of 250 rpm s<sup>-1</sup>. Spin speed of 6000 rpm for 20 s with a ramp-up of 2000 rpm s<sup>-1</sup> was followed for the second-step and 300  $\mu$ L chlorobenzene was dropped on the spinning substrates during the second spin-coating step at 5 s before the end of the procedure. The substrate was then immediately transferred on a hotplate and heated at 100 °C for 20 min.

**J–V Characterization and EQE Measurements:** Photovoltaic performances of the devices were determined using Keithley 2400 source under AM 1.5G illumination (Sciencetech class 3A) of 100 mW cm<sup>-2</sup> with 1100 nm long-wave-pass silicon filter in N<sub>2</sub> atmosphere. An aperture (active area 0.049 cm<sup>2</sup>) was used for measurement. The spectral mismatch was calibrated by a reference solar cell (Newport). We corrected for spectral mismatch between our lamp and AM 1.5G.<sup>[20]</sup> EQE spectra were obtained from under monochromatic illumination (400 W Xe lamp equipped with a monochromator and cut-off filters) after the correction of power with Newport 818-UV and Newport 838-IR photodetectors. The current response was obtained with a Lakeshore preamplifier connected to a Stanford Research 830 lock-in amplifier.

**Characterization:** UPS spectra are obtained on ITO/ZnO substrates. Photoelectron spectroscopy was carried out in a PHI5500 Multi-Technique system with nonmonochromatized He-I $\alpha$  radiation (UPS) ( $h\nu = 21.22$  eV). Optical absorption measurements were obtained from a UV–vis–IR spectrophotometer (Lambda 950). Field-emission scanning electron microscopy (FE-SEM, Hitachi SU8230) was employed for morphological and structural characterization.

## Supporting Information

Supporting Information is available from the Wiley Online Library or from the author.

## Acknowledgements

This research was supported by Ontario Research Fund-Research Excellence program (ORF7-Ministry of Research and Innovation, Ontario Research Fund-Research Excellence Round 7); and by the Natural Sciences and Engineering Research Council (NSERC) of Canada. M.I.S. acknowledges the support of Banting Postdoctoral Fellowship Program, administered by the Government of Canada. The authors thank L. Levina, R. Wolowiec, D. Kopilovic, and E. Palmiano for their help over the course of this research.

## Conflict of Interest

The authors declare no conflict of interest.

## Keywords

4-terminal tandem, graded, infrared, quantum dot solar cells

Received: June 16, 2018

Revised: August 21, 2018

Published online:

- [1] M. Yuan, M. Liu, E. H. Sargent, *Nat. Energy* **2016**, *1*, 16016.
- [2] Z. Ning, O. Voznyy, J. Pan, S. Hoogland, V. Adinolfi, J. Xu, M. Li, A. R. Kirmani, J. P. Sun, J. Minor, K. W. Kemp, H. Dong, L. Rollny, A. Labelle, G. Carey, B. Sutherland, I. Hill, A. Amassian, H. Liu, J. Tang, O. M. Bakr, E. H. Sargent, *Nat. Mater.* **2014**, *13*, 822.
- [3] R. Wang, Y. Shang, P. Kanjanaboos, W. Zhou, Z. Ning, E. H. Sargent, *Energy Environ. Sci.* **2016**, *9*, 1130.
- [4] F. P. García De Arquer, A. Armin, P. Meredith, E. H. Sargent, *Nat. Rev. Mater.* **2017**, *2*, 1.
- [5] V. Sukhovatkin, S. Hinds, L. Brzozowski, E. H. Sargent, *Science* **2009**, *324*, 1542.
- [6] S. Y. Jeong, S. C. Lim, D. J. Bae, Y. H. Lee, H. J. Shin, S. M. Yoon, J. Y. Choi, O. H. Cha, M. S. Jeong, D. Perello, M. Yun, *Appl. Phys. Lett.* **2008**, *92*, 1.
- [7] V. Wood, M. J. Panzer, J. Chen, M. S. Bradley, J. E. Halpert, M. G. Bawendi, V. Bulović, *Adv. Mater.* **2009**, *21*, 2151.
- [8] C.-H. M. Chuang, P. R. Brown, V. Bulović, M. G. Bawendi, *Nat. Mater.* **2014**, *13*, 796.
- [9] X. Lan, S. Masala, E. H. Sargent, *Nat. Mater.* **2014**, *13*, 233.
- [10] A. H. Ip, A. Kiani, I. J. Kramer, O. Voznyy, H. F. Movahed, L. Levina, M. M. Adachi, S. Hoogland, E. H. Sargent, *ACS Nano* **2015**, *9*, 8833.
- [11] M. Liu, O. Voznyy, R. Sabatini, F. P. García De Arquer, R. Munir, A. H. Balawi, X. Lan, F. Fan, G. Walters, A. R. Kirmani, S. Hoogland, F. Laquai, A. Amassian, E. H. Sargent, *Nat. Mater.* **2017**, *16*, 258.
- [12] Y. Cao, A. Stavrinadis, T. Lasanta, D. So, G. Konstantatos, *Nat. Energy* **2016**, *1*, 16035.
- [13] H. Aqoma, S.-Y. Jang, *Energy Environ. Sci.* **2018**, *11*, 1603.
- [14] J. Choi, Y. Kim, J. W. Jo, J. Kim, B. Sun, G. Walters, F. P. García de Arquer, R. Quintero-Bermudez, Y. Li, C. S. Tan, L. N. Quan, A. P. T. Kam, S. Hoogland, Z. Lu, O. Voznyy, E. H. Sargent, *Adv. Mater.* **2017**, *29*, 1.
- [15] X. Zhang, J. Zhang, D. Phuyal, J. Du, L. Tian, V. A. Öberg, M. B. Johansson, U. B. Cappel, O. Karis, J. Liu, H. Rensmo, G. Boschloo, E. M. J. Johansson, *Adv. Energy Mater.* **2017**, *1702049*, 1702049.
- [16] M. Liu, F. P. G. De Arquer, Y. Li, X. Lan, G. H. Kim, O. Voznyy, L. K. Jagadamma, A. S. Abbas, S. Hoogland, Z. Lu, J. Y. Kim, A. Amassian, E. H. Sargent, *Adv. Mater.* **2016**, *28*, 4142.
- [17] F. Xu, X. Ma, C. R. Haughn, J. Benavides, M. F. Doty, S. G. Cloutier, *ACS Nano* **2011**, *5*, 9950.
- [18] V. Adinolfi, Z. Ning, J. Xu, S. Masala, D. Zhitomirsky, S. M. Thon, E. H. Sargent, *Appl. Phys. Lett.* **2013**, *103*, 011106.
- [19] I. J. Kramer, L. Levina, R. Debnath, D. Zhitomirsky, E. H. Sargent, *Nano Lett.* **2011**, *11*, 3701.
- [20] J. Y. Kim, V. Adinolfi, B. R. Sutherland, O. Voznyy, S. J. Kwon, T. W. Kim, J. Kim, H. Ihee, K. Kemp, M. Adachi, M. Yuan, I. Kramer, D. Zhitomirsky, S. Hoogland, E. H. Sargent, *Nat. Commun.* **2015**, *6*, 1.
- [21] Y. Kim, K. Bicanic, H. Tan, O. Ouellette, B. R. Sutherland, F. P. García De Arquer, J. W. Jo, M. Liu, B. Sun, M. Liu, S. Hoogland, E. H. Sargent, *Nano Lett.* **2017**, *17*, 2349.
- [22] Y. Chen, X. L. Gong, J. G. Gai, *Adv. Sci.* **2016**, *3*, 1.
- [23] Y. C. Lin, C. C. Lu, C. H. Yeh, C. Jin, K. Suenaga, P. W. Chiu, *Nano Lett.* **2012**, *12*, 414.
- [24] NREL best research-cell efficiencies: solar-cell efficiency chart, <https://www.nrel.gov/pv/assets/pdfs/pv-efficiencies-07-17-2018.pdf> (accessed: August 2018).
- [25] M. I. Bodnarchuk, S. Yakunin, L. Piveteau, M. V. Kovalenko, *Nat. Commun.* **2015**, *6*, 1.
- [26] M. A. Boles, D. Ling, T. Hyeon, D. V. Talapin, *Nat. Mater.* **2016**, *15*, 364.
- [27] N. Ahn, D. Y. Son, I. H. Jang, S. M. Kang, M. Choi, N. G. Park, *J. Am. Chem. Soc.* **2015**, *137*, 8696.
- [28] Y. Bi, S. Pradhan, S. Gupta, M. Z. Akgul, A. Stavrinadis, G. Konstantatos, *Adv. Mater.* **2018**, *30*, 1.
- [29] A. Karani, L. Yang, S. Bai, M. H. Futscher, H. J. Snaith, B. Ehrler, N. C. Greenham, D. Di, *ACS Energy Lett.* **2018**, *3*, 869.
- [30] M. Saliba, T. Matsui, J.-Y. Seo, K. Domanski, J.-P. Correa-Baena, M. K. Nazeeruddin, S. M. Zakeeruddin, W. Tress, A. Abate, A. Hagfeldt, M. Grätzel, *Energy Environ. Sci.* **2016**, *9*, 1989.
- [31] H. Tan, A. Jain, O. Voznyy, X. Lan, F. P. García de Arquer, J. Z. Fan, R. Quintero-Bermudez, M. Yuan, B. Zhang, Y. Zhao, F. Fan, P. Li, L. N. Quan, Y. Zhao, Z.-H. Lu, Z. Yang, S. Hoogland, E. H. Sargent, *Science* **2017**, *355*, 722.
- [32] D. Zhao, C. Wang, Z. Song, Y. Yu, C. Chen, X. Zhao, K. Zhu, Y. Yan, *ACS Energy Lett.* **2018**, *3*, 305.
- [33] J. Kim, M. I. Saidaminov, H. Tan, Y. Zhao, Y. Kim, J. Choi, J. W. Jo, J. Fan, R. Quintero-Bermudez, Z. Yang, L. N. Quan, M. Wei, O. Voznyy, E. H. Sargent, *Adv. Mater.* **2018**, *30*, 1.